Martinelli et al., http://www.jcb.org/cgi/content/full/jcb.201209077/DC1

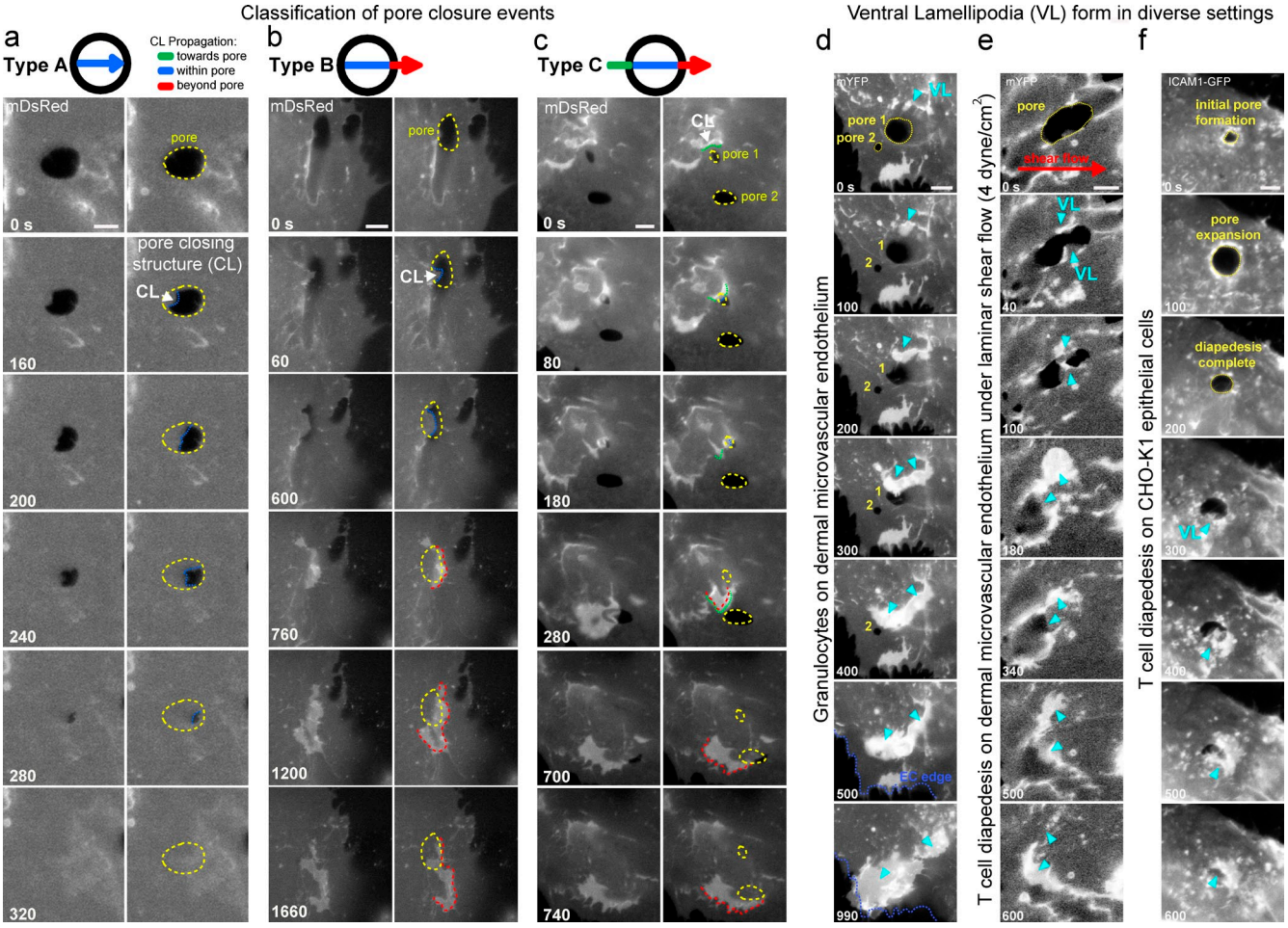

Figure S1. **Classification of pore closure events in diverse settings.** Classification of pore closure events. Live-cell imaging of pore closure after lymphocyte diapedesis across MVECs expressing mDsRed. Yellow dashed lines indicate the open pore in the endothelium. Dashed blue lines indicate propagation of closing protrusions within the pore. Green and red lines, respectively, represent phases of protrusion propagation outside of the pore moving toward it before closure or away from it afterward. (a) A representative type A closure. Propagation occurs within the confines of the pore only, moving from one edge to the opposite one. (b) A representative type B closure. Protrusion initiates at a pore edge and continues to propagate beyond the distal edge of the pore after closing it. Note that in the selected example the protrusion is initiated well before the T cell has completely exited the pore. (c) A representative type C closure. Protrusion initiates distant from the pore and migrates toward, across, and beyond it. Note that the selected event is also an example of successive propagation across and closure of two adjacent pores (pore 1 and 2). See also Video 2, Part I. Closure proceeds similarly through VL in diverse settings. (d) Live-cell imaging during granulocyte transcellular diapedesis across mYFP-expressing MVECs. Note that the VL (arrowheads) initiates distant from one pore, travels across (and closes) two distinct pores (1 and 2) in succession, and continues to extend beyond the edge of the cell (dashed blue line) to close a paracellular gap (type C closure). (e) Diapedesis as in A, performed with T cells under physiological laminar fluid shear flow (4 dyne/cm^2; red arrow). Note that two distinct VL form on opposite sides of the pore to close it and continue propagation briefly (type B closure). (f) Transcellular diapedesis of T cells across CHO-K1 epithelial cells expressing ICAM-1-GFP. Note VL initiates slightly outside of, and continues to propagate beyond, the pore (type C closure). Arrowheads indicate pore-closing VL. See also Video 2, Part II. Bars, 5 µm.

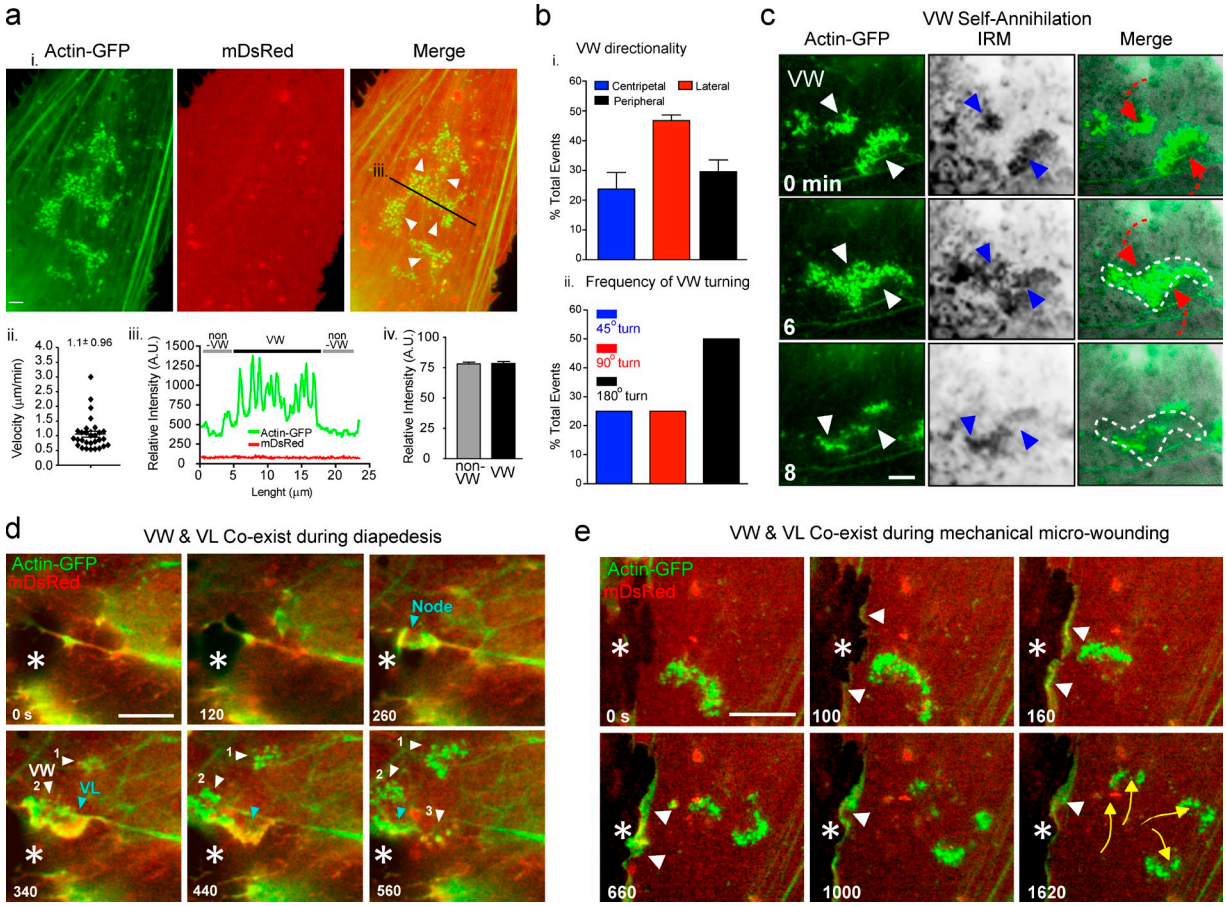

Figure S2. **VL coexist with VW in endothelial cells.** (a) MVECs transfected with mDsRed and actin-GFP were imaged live in the absence of leukocytes, TNF pretreatment, or any other stimulus. Representative images (from >30 separate samples) show spontaneously formed actin waves (WV) characterized by actin punctae (i) that traveled ~1 µm/min (ii) without membrane protrusion (iii). (i) Fluorescence intensity line scan from right panel shows that peaks in the actin signal (green line), which correspond to individual actin punctae of a wave, are not coupled to changes in the membrane intensity (red line). (iv) Quantification of membrane fluorescence intensity in non-VW and VW ROIs. Values represent means ± SEM (n > 10). (b) Quantitative analysis of VW propagation directionality with respect to endothelial cell axes of symmetry (i). Values represent means ± SEM (n = 3). (ii.) The frequency of ~45°, ~90°, and ~180° turns during VW propagation was determined from analysis of >50 micro-wound closure events. (c) Combined fluorescence microscopy (left) and IRM (middle, arrowheads) of MVECs transfected with actin-GFP and mDsRed (not depicted) shows that these waves protrude ventrally against the substrate and exhibit swirling propagation (red arrowheads and dashed line) and self-annihilation upon intersection (white dotted line). (d) Imaging of actin dynamics during closure of a lymphocyte diapedesis pore (asterisks) showing that VL initiate from nodes of actin accumulated on preformed fibers (cyan arrowheads). Additionally, VW (white arrowheads) propagate independently from (1) and coordinately with (2 and 3) VL during pore closing events. See also Video 4, Part I, ex. 3. (e) Imaging of actin dynamics during mechanical micro-wound closure shows coexistence of wound-responsive VL (white arrowheads) and nonresponsive VW (yellow arrows). Asterisk indicates site of mechanical probe wounding of a neighbor cell.

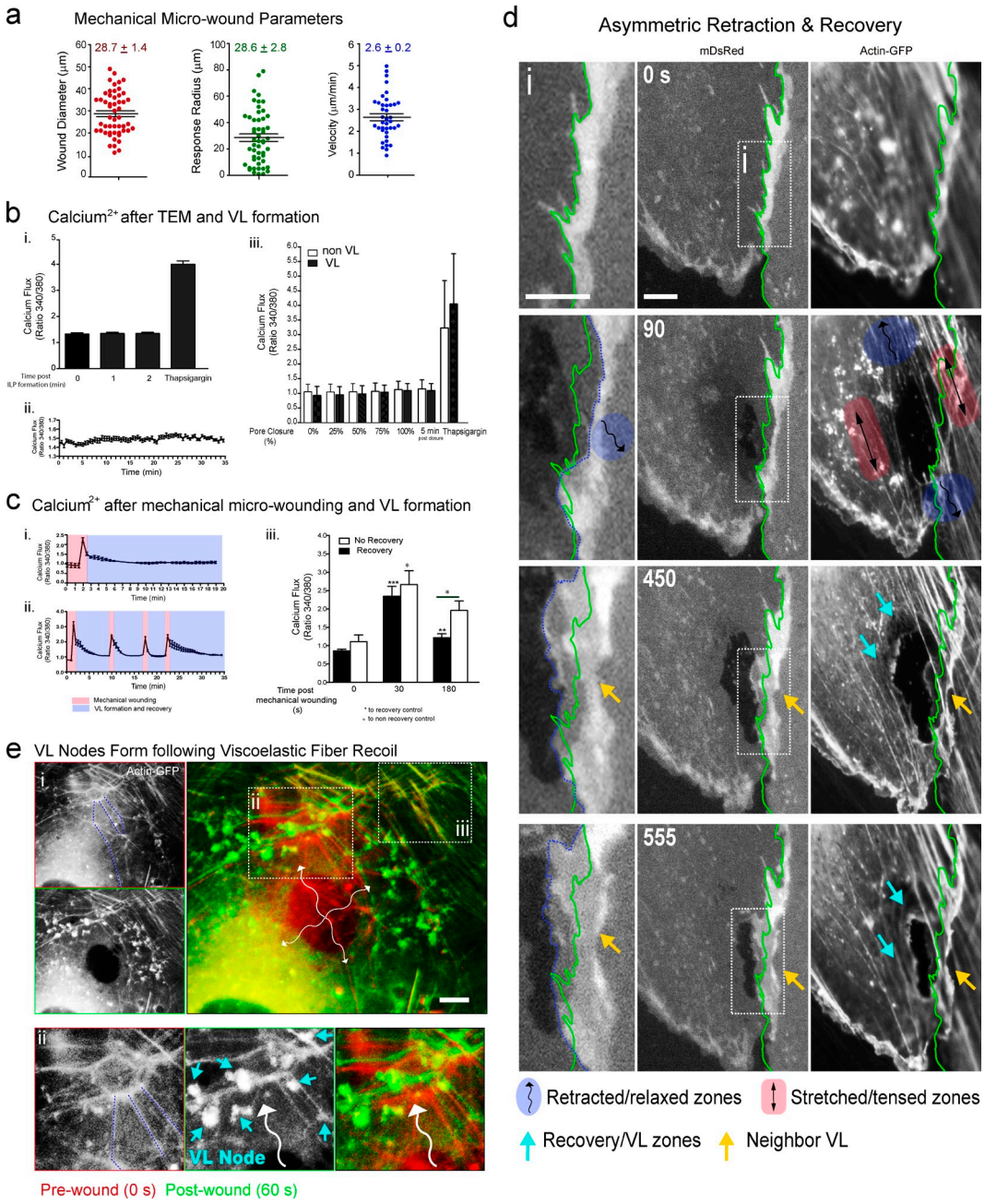

Figure S3. **Mechanical micro-wounding and response to tension breakage.** (a) Quantitative analysis of mechanical micro-wounding and response parameters. (b) Calcium responses during leukocyte diapedesis and mechanical micro-wounding pore closure. MVECs transfected with mDsRed and actin-GFP were loaded with Fura-2AM and then imaged during leukocyte diapedesis (b) or mechanical micro-wounding (c). (b, i) Calcium responses (measured as ratio 340:380) in the imaging frame immediately before (0), in the two frames (1 and 2, taken at 20 s intervals) after initial leukocyte-mediated transcellular pore formation, or in the frame immediately after addition of thapsigargin (positive control). $n = 3$. (ii) Calcium flux recorded continuously during persistent leukocyte diapedesis over a 35-min duration. $n = 3$. (iii) Calcium ratios were calculated at different stages of pore closure (i.e., percentage of completion) for VL and non-VL areas. $n = 8$. (c) Calcium responses were recording during single (i) and multiple sequential (ii) mechanical micro-wounding events. Blue regions represent the time frames corresponding to the initiation of VL and onset of pore closure. Failure to close pores correlated with failure to normalize calcium. Calcium ratios at 30 and 180 s after mechanical micro-wounding are shown. (iii) Non-closing pores failed to normalize calcium significantly below a ratio of 2. Values represent means ± SEM ($n > 3$). Statistical significance is indicated with p-values as follows: ***, $P < 0.001$; **, $P < 0.01$; *, $P < 0.05$. (d) Asymmetric retraction and recovery of mechanical micro-wounds. Wounding in a region of parallel actin stress fibers results in asymmetric viscoelastic recoil/relaxation in discrete regions (shaded blue) in antiparallel directions. Adjacent untouched fibers undergo visible extension, presumably because of compensatory force loading (red shaded areas). Robust VL and VW recovery responses predominantly formed in the relaxed (cyan arrows) but not the stretched areas (red shading). Dashed green and blue lines, respectively, indicate the original and current position of the intercellular junction adjacent to the transcellular micro-wound. At 90 s after wounding, a substantial degree of retraction of the intact junction toward the untouched neighbor is evident. Strong localized VL responses were seen from the neighbor precisely at the site of the initial relaxation (yellow arrow), formed within 80 s of micro-wounding (not depicted) and sustained at 450 and 555 s later. See also corresponding Video 6 and compare/contrast with Fig. 7 a. (e) Zones of viscoelastic recoil in actin networks form nodes of VL initiation on intact fibers. Images of actin-GFP immediately before and after micro-wounding were differentially pseudo-colored and overlaid. This representation highlights the displacement of intact actin networks at sites distant from, but originally tethered to, fibers that were broken during wounding. These highly displaced fibers become preferential loci for accumulation of actin nodes and VL (cyan arrows). See Video 7, ex. 2. Bars, 5 µm.

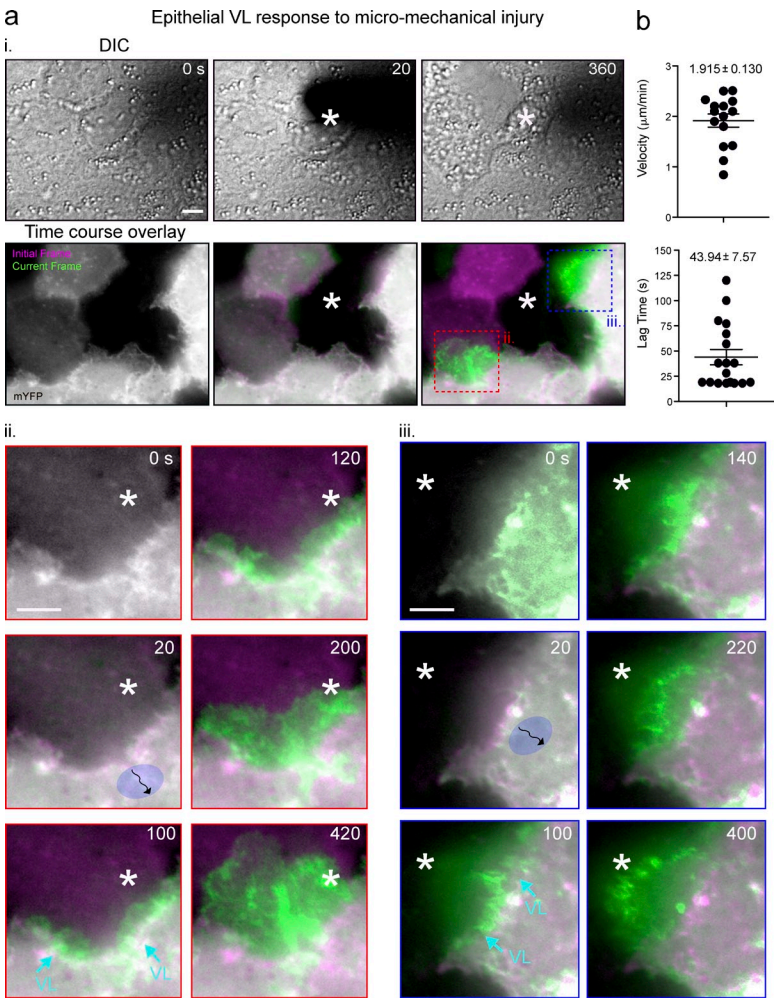

Figure S4. **Epithelial VL response after mechanical micro-wounding.** MDCK cells transfected with mDsRed and actin-GFP were imaged live during mechanical micro-wound recovery. (a, i, top) DIC images of a confluent monolayer being probe wounded (dark area, asterisk). (bottom) Actin-GFP fluorescence (of the positive transfectants within the monolayer) with the initial (magenta) and subsequent (green) time points overlayed. (ii and iii) Zoomed regions showing additional time points of boxed areas in i. Note that immediately after wounding a narrow magenta region is evident at the edges of the cell facing the wound, indicating cell retraction. In subsequent frames strong green signal of VL (cyan arrows) spreading toward the wound are evident. (b) Quantification of epithelial VL propagation velocity and lag time until formation of first VL after micro-wound. Values represent means ± SEM (n > 30). Bars, 5 µm.

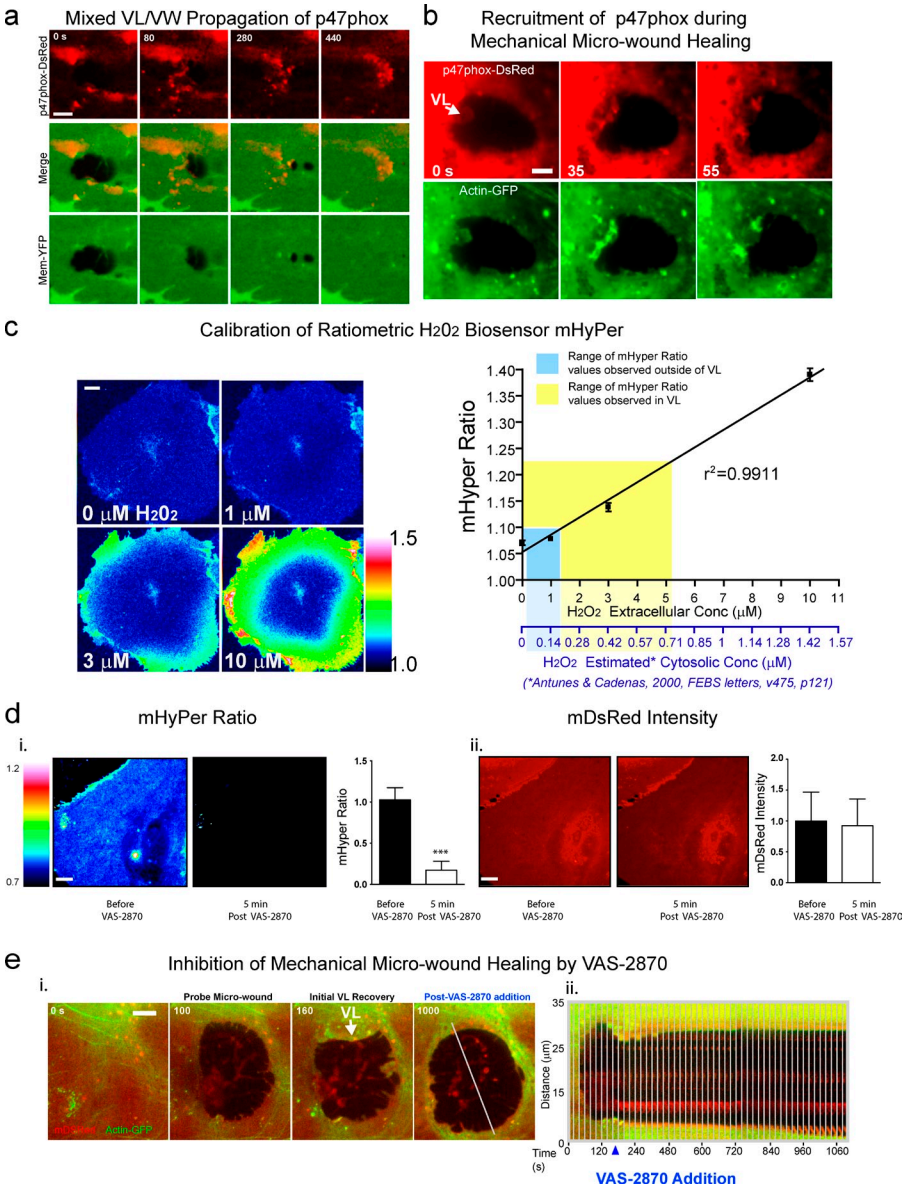

Figure S5. **Characterizing p47phox and H_2O_2 production in micro-wound healing.** (a) Closure of a transcellular pore in MVECs coexpressing mYFP and p47phox-DsRed. Note enrichment of p47phox both in the VL leading edge (see 80 s) and in VW type punctae that continue to propagate after pore closure (280 and 440 s). (b) Representative closure of a mechanical micro-wound in MVEC coexpressing actin-GFP and p47phox-DsRed. White arrow indicates an actin-rich VL with colocalized enrichment of p47phox. (c) MVECs expressing mHyPer were subjected to ratiometric imaging upon addition of the indicated concentrations of exogenous H_2O_2 (left). Mean ratios were calculated for each concentration and plotted against the corresponding concentration of H_2O_2 and subjected to linear regression (right). The estimated intracellular concentration of H_2O_2 is known to be approximately one seventh of that which is added exogenously (Antunes and Cadenas, 2000). Based on this, an estimated intracellular H_2O_2 x-axis scale is shown. Colorimetric range indicators show the observed VL (yellow) and non-VL (blue) mHyPer ratios and the corresponding estimation of intracellular H_2O_2 concentrations that they reflect. (d) MVECs coexpressing mHyPer and mDsRed were imaged before and 5 min after addition of 15 μM VAS-2870. Representative images and quantitation of mHyper ratios (i) and mDsRed intensity (ii) are shown (n = 3). Statistical significance is indicated with p-value: ***, $P < 0.001$. Error bars represent SEM. (e) Representative blockade of VL and wound healing after probe-induced micro-wounding of MVEC coexpressing mDsRed and actin-GFP. Selected frames show MVEC immediately before and after micro-wounding, after initiation of VL, and after addition of the NADPH oxidase inhibitor VAS-2870 (left). White line shows position used to generate a kymograph (right). Note that VL immediately retract and wound fails to close after addition of VAS-2870. Bars, 5 μm.

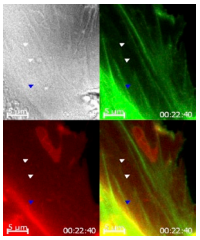

Video 1. **Leukocyte-driven endothelial micro-wounds are closed efficiently.** (Part I) Directed lamellipodia heal leukocyte-mediated vascular micro-wounds. Live-cell imaging of lymphocyte diapedesis on MVECs transfected with actin-GFP (green) and mDsRed (red), corresponding to Fig. 1 b. Boxed regions A and B are expanded in bottom panels. (A) A burst of lamellar activity that rapidly closes a transcellular migration pore immediately after completion of diapedesis, which continues to travel a significant distance beyond the pore. Boxed region B and asterisk in top panel show related processes during closure of paracellular diapedesis gaps (see Fig. 3 for further explanation). (Part II) Membrane doubling/folding is associated with closing lamellipodia. Live-cell imaging of lymphocyte transcellular diapedesis across MVECs transfected with actin-GFP (green) and mDsRed (red) corresponding to Fig. 1 e. Arrowheads indicate initiation of actin protrusions at the edge of the pore (white) and adjacent to it (blue), which seem to emerge from preformed fibers, as the leukocyte completes diapedesis. These expand quickly and propagated across the pore to the MVEC cell periphery in coordination with lymphocyte movement between the cell and the substratum. The clearly evident doubling of the fluorescence membrane signal around these structures demonstrates that membrane is folded around them and that they are propagating as frank membrane protrusions. Images were acquired by time-lapse microscopy using a microscope (Axiovert 200M; Carl Zeiss). Frames were taken every 30 s for 26 min (Part I) or 20 s for 22 min and 40 s (Part II).

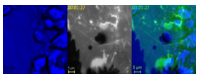

Video 2. **Classification of closing lamellipodia in diverse settings.** (Part I) Live-cell imaging of pore closure after lymphocyte diapedesis across MVECs expressing mYFP, corresponding to Fig. S1 (a–c). Representative examples of type A, B, and C pore closures are shown sequentially. (Part II) Live-cell imaging of transmigration in three distinct settings corresponding to Fig. S1 (d–f). Example 1 shows a granulocytes migrating across a MVEC expressing mYFP and successive closure of two distinct pores by a single VL. Example 2 shows transcellular migration of a T cell under 4 dyne/cm^2 laminar fluid shear flow and closure of a single pore by two distinct VL traveling in opposite directions. Example 3 shows transcellular diapedesis of a lymphocyte across an ICAM-1-GFP–expressing CHO-K1 epithelial cell, which is closed by a VL-mediated process not unlike those seen in MVECs. Images were acquired by time-lapse microscopy using a microscope (Axiovert 200M; Carl Zeiss). Frames were taken every 25 s for 4 min and 45 s (type A), 20 s for 28 min and 40 s (type B), 20 s for 14 min and 40 s (type C), 25 s for 10 min (Part II, ex. 1), 25 s for 26 min and 5 s (Part II, ex. 2), or 22 s for 28 min and 8 s (Part II, ex. 3).

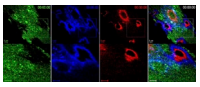

Video 3. **VL heal endothelial micro-wounds.** Live-cell serial-section spinning disk confocal imaging of lymphocytes migrating on MVECs expressing m-YFP, corresponding to Fig. 2 b. Time-lapse video shows select basal/ventral (green), intermediate (blue), and apical/dorsal (red) confocal sections both separately and overlaid. A wide-field view showing five separate transmigration pore closure events (as well as several gap closures) and a zoomed in view of three of them is shown sequentially. Note that lamellar structures are clearly, and exclusively, ventral (i.e., green) spread out under the pores (initially visibly open in the intermediate and dorsal section), effectively closing them from the bottom. Images were acquired by time-lapse microscopy using a spinning disk confocal microscope (Axiovert 200M; Carl Zeiss). Frames were taken every 20 s for 6 min and 40 s.

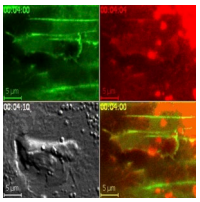

Video 4. **Complex features of VL initiation and propagation.** (Part I) VL form at site of preexisting actin filaments. Live-cell imaging of lymphocyte migration on MVECs transfected with actin-GFP (green) and mDsRed (red), corresponding to Fig. 4. In three sequential examples, extensive and complex micro-distortions of membrane and actin cytoskeleton are generated in MVECs by T cells as they form migration pores and spread under the endothelium (disrupting MVEC–substrate adhesion in the process). In all cases, preformed actin filaments in the distortion zone serve as predominant VL nucleation sites whereby a node or quasi-orthogonal spike appears briefly (~20–40 s) and then abruptly transitions to a VL. Additionally, some evidence for both independent and coordinated VL and VW propagation can be seen in example 3 (see Fig. S2 d and legend for details). (Part II) Directional propagation features of VL. Live-cell imaging of lymphocyte migration on MVECs transfected with mDsRed (red; and, in ex. 3, actin-GFP [green] as well) corresponding to Fig. 5. Example 1 shows closure of a single pore by two distinct VL traveling in opposite directions (corresponding to Fig. 5 b). Example 2 shows sequential closure of a transcellular pore and a paracellular gap by a single VL. This VL initially turns nearly 180° to close the pore and subsequently adjusts ~90° in the opposite direction to steer toward and close the gap (corresponding to Fig. 5 d). Example 3 shows a larger field of view in which multiple diapedesis pores and gaps are formed in mDsRed (red)- and actin-GFP (green)–expressing MVECs (corresponding to Fig. 5 f). This video provides a representative of the ability of the endothelium to coordinate complex propagation of multiple VL to close concomitantly formed discontinuities. Also note the apparent mixed VL and VW propagation, whereby VW seem to persist after micro-wound closure and VL extinction. Images were acquired by time-lapse microscopy using a microscope (Axiovert 200M; Carl Zeiss). Frames were taken every 20 s for 13 min and 40 s (Part I, ex. 1), 20 s for 11 min and 20 s (Part I, ex. 2), 22 s for 24 min and 22 s (Part I, ex. 3), 20 s for 14 min and 20 s (Part II, ex. 1), 20 s for 27 min and 30 s (Part II, ex. 2), or 20 s for 15 min and 10 s (Part II, ex. 3).

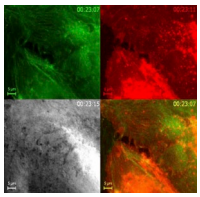

Video 5. **Closure events after mechanical micro-wounding.** (Part I) Sequential transcellular micromechanical wounding and healing events in a single MVEC. Live-cell imaging of transcellular mechanical micro-wounding in an MVEC transfected with actin-GFP (green) and mDsRed (red), corresponding to Fig. 6 b. A single MVEC was subjected to four sequential mechanical micro-wounding events (see numbers in bottom right panel). Each time the initial wound rapidly expands as broken adhesions and cytoskeleton caused viscoelastic recoil of preexisting tension. The MVEC then rapidly formed nodes of actin in a large ~20–30-µm radius around the pore with mixed VL and VW features. These exhibit directed propagation into the micro-wound to close it. The ventral nature of these structures can clearly be seen by dark regions in IRM (bottom left). Bars, 5 µm. (Part II) Closure event after paracellular mechanical micro-wounding. Live-cell imaging of paracellular mechanical micro-wound in MVEC transfected with actin-GFP (green) and mDsRed (red). By placing the probe tip over one cell near its junction a paracellular gap is formed. Significant viscoelastic recoil is evident in both the wounded cell and the untouched neighbor (particularly evident in the bottom right corner) that correlates with a highly robust VL and VW recovery response. The ventral nature of these structures can be seen by the appearance of dark spots in IRM (bottom left). Bars, 5 µm. Images were acquired by time-lapse microscopy using a microscope (Axiovert 200M; Carl Zeiss). Frames were taken every 20 s for 45 min (Part I) or 20 s for 28 min and 20 s (Part II).

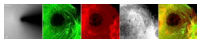

Video 6. **Asymmetric retraction and recovery after mechanical micro-wounding.** Live-cell imaging of transcellular mechanical wounding in MVECs coexpressing actin-GFP (green) and mDsRed (red), corresponding to Fig. 7 a and Fig. S3 d. Whereas the first example shows both predominant retraction and subsequent VL/VW recovery in orthogonally oriented directions (i.e., toward the top and bottom left corners), in the second example retraction and recovery both predominantly occur in antiparallel directions (i.e., toward the top left and bottom right corners). In both cases the nonresponding regions opposite the major recoil/response areas are visibly stretched and, therefore, tensed during wounding. In both examples the broken isometric tension is visibly transmitted to discrete regions of the unwounded neighbor cells through intact adherens junctions that retract and translate toward the neighboring cell (right side). In response, the untouched cells produce an avid VL response precisely in the location where retraction occurred. The ventral nature of these response structures is shown by the appearance of dark spots in IRM (fourth panel). Bars, 5 µm. Images were acquired by time-lapse microscopy using a microscope (Axiovert 200M; Carl Zeiss). Frames were taken every 20 s for 19 min and 20 s (ex. 1) or 20 s for 14 min and 40 s (ex. 2).

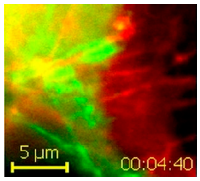

Video 7. **Tension release correlates with VL initiation on actin filaments.** Live-cell imaging of mechanical wounding in MVECs coexpressing actin-GFP and mDsRed (not depicted), corresponding to Figs. 7 b and S3 e. MVECs were mechanically wounded paracellularly (ex. 1) or transcellulary (ex. 2). To better understand the relationship between the viscoelastic recoil that develops rapidly in the cytoskeleton after wounding, and the subsequent formation of actin nodes and VL, we froze the prewound actin image into the left panel and the red channel of the right panel and placed the full dynamic time-lapse series in the middle panels and green channel of the right panel. In the color overlaid panel on the right, the first frame has time-matched green and red images that show perfect colocalization yielding a yellow image. After micro-wound the progressive time series images in green become separated from the original alignment for an intuitive visualization of recoil response. Areas that undergo the most significant retraction exhibit predominant formation of nodes and VL (which were confirmed as such via IRM and membrane signal (acquired but not depicted). Images were acquired by time-lapse microscopy using a microscope (Axiovert 200M; Carl Zeiss). Frames were taken every 20 s for 9 min (ex. 1) or 15 s for 6 min (ex. 2).

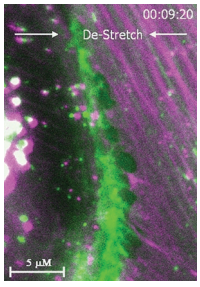

Video 8. **Enforced substrate compression initiates putative VL.** Live-cell imaging of a confluent MVEC monolayer coexpressing actin-GFP and mYFP during an acute 10% uniaxial compression/de-stretch of the substrate, corresponding to Fig. 8 b (ii). To better visualize the initial de-stretch and the subsequent VL formation, we froze the first frame (magenta) and superimposed the time-lapsed images (green). Putative VL activity can be seen emanating from the ends of actin filaments that are partially aligned with the axis of de-stretch. For individual filaments, note the similarity to Video 1 B, showing paracellular gap closure after diapedesis micro-wounding. Shown is one representative experiment of at least 10 independent experiments. Images were acquired by time-lapse microscopy using a microscope (Axiovert 200M; Carl Zeiss). Frames were taken every 35 s for 11 min and 45 s

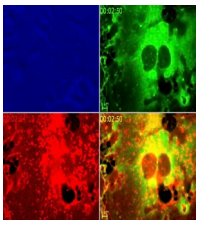

Video 9. **Role of Rho-GTPases on pore closure.** (Part I) Effect of Rac1 inhibitor NSC23766 on pore closure. Representative live-cell imaging of reversible VL inhibition during diapedesis on MVECs expressing mYFP that is analogous to Fig. 9 c. In initial frames, six diapedesis events can be seen in progress. At 5 min, as indicated, the Rac1 inhibitor NSC23677 (500 μM) was added. Over the next ∼18 min all of the original pores and gaps, as well as some additionally formed micro-wounds, are present, despite completion of most of the diapedesis events. After drug washout the accumulated micro-wounds were rapidly closed by a concerted mobilization of multiple independent and steered VL. (Part II) Effect of Rho kinase inhibitor Y27632 on micro-wound healing. Live-cell imaging of T cell diapedesis on MVECs coexpressing mDsRed (red) and actin-GFP (green) during addition of the Rho kinase inhibitor Y27632. During the initial 5 min, in the setting of high lymphocyte density, multiple diapedesis events are seen at various stages and some VL have formed to initiate pore closure. During addition of Y27632 (90 μM), robust steered VL closure activity proceeds uninterrupted for >25 min, progressively closing each micro-wound as individual diapedesis events reach completion. Separate studies in the absence of leukocytes confirm that drug is active at this concentration at reducing stress fiber density within minutes of addition (not depicted). Bars, 5 μm. Images were acquired by time-lapse microscopy using a microscope (Axiovert 200M; Carl Zeiss). Frames were taken every 20 s for 50 min and 50 s (Part I) or 20 s for 31 min and 50 s (Part II).

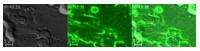

Video 10. **ROS play a role in VL propagation.** (Part I) The NADPH oxidase subunit p47phox is enriched in VL. Representative live-cell imaging of p47phox distribution dynamics during diapedesis. MVECs were cotransfected with p47phox-DsRed (red) and either mYFP (green; ex. 1) or actin-GFP (green; ex. 2, corresponding to Fig. 10 a). Example 1 shows leading edge enrichment of p47phox in VL during closure of a paracellular gap. Example 2 shows p47phox coenriched with actin at nodes of VL initiation and in VL leading edge, which propagate successively across a transcellular pore and then a paracellular gap. IRM shown on the far right indicates VL initiate and propagate in close apposition to the substrate. (Part II) Effect of ROS inhibitors on VL-mediated pore closure. Representative live-cell imaging of reversible blockade of VL by ROS inhibitors during diapedesis corresponding to Fig. 10 d. MVECs expressing mYFP were imaged during lymphocyte diapedesis. Where indicated, inhibitors of NAPDH oxidase signaling apocynin (1 mM; ex. 1) or Tempol (500 μM; ex. 2) were added and then at later times washed out (as indicated). In both cases micro-wounds remained patent during the 15-min incubation with drug, and washout led to immediate mobilization of steered VL and micro-wound healing. Images were acquired by time-lapse microscopy using a microscope (Axiovert 200M; Carl Zeiss). Frames were taken every 25 s for 29 min and 5 s (Part I, ex. 1), 20 s for 12 min and 5 s (Part I, ex. 2), 45 s for 46 min and 45 s (Part II, ex. 1), or 45 s for 42 min and 25 s (Part II, ex. 2).

Reference

Antunes, F., and E. Cadenas. 2000. Estimation of H_2O_2 gradients across biomembranes. *FEBS Lett.* 475:121–126. http://dx.doi.org/10.1016/S0014-5793(00)01638-0